Fast spatial beam shaping by acousto-optic diffraction for 3D non-linear microscopy

Walther Akemann, Jean-François Léger, Cathie Ventalon, Benjamin Mathieu, Stéphane Dieudonné, Laurent Bourdieu

Fast spatial beam shaping by acousto-optic diffraction for 3D non-linear microscopy

Walther Akemann,[1,2,3] Jean-François Léger,[1,2,3] Cathie Ventalon,[1,2,3] Benjamin Mathieu,[1,2,3] Stéphane Dieudonné,[1,2,3] and Laurent Bourdieu[1,2,3,*]

[1]*Ecole Normale Supérieure, Institut de Biologie de l'ENS (IBENS), 46 rue d'Ulm, Paris, F-75005 France*
[2]*Inserm, U1024, Paris, F-75005 France*
[3]*CNRS, UMR 8197, Paris, F-75005 France*
[*]*laurent.bourdieu@ens.fr*

Abstract: Acousto-optic deflection (AOD) devices offer unprecedented fast control of the entire spatial structure of light beams, most notably their phase. AOD light modulation of ultra-short laser pulses, however, is not straightforward to implement because of intrinsic chromatic dispersion and non-stationarity of acousto-optic diffraction. While schemes exist to compensate chromatic dispersion, non-stationarity remains an obstacle. In this work we demonstrate an efficient AOD light modulator for stable phase modulation using time-locked generation of frequency-modulated acoustic waves at the full repetition rate of a high power laser pulse amplifier of 80 kHz. We establish the non-local relationship between the optical phase and the generating acoustic frequency function and verify the system for temporal stability, phase accuracy and generation of non-linear two-dimensional phase functions.

OCIS codes: (070.6120) Spatial light modulators; (110.1080) Active or adaptive optics; (120.5800) Scanners; (140.3300) Laser beam shaping; (180.4315) Nonlinear microscopy; (230.1040) Acousto-optical devices.

References and links

1. J. Xu and R. Stroud, *Acousto-Optic Devices: Principles, Design and Applications* (John Wiley, 1992).
2. E. H. Young and S. K. Yao, "Design Considerations for Acoustooptic Devices," Proc. Ieee **69,** 54-64 (1981).
3. A. Vanderlugt and A. M. Bardos, "Design relationships for acoustooptic scanning systems," Appl. Optics **31,** 4058-4068 (1992).
4. A. Kaplan, N. Friedman, and N. Davidson, "Acousto-optic lens with very fast focus scanning," Opt. Lett. **26,** 1078-1080 (2001).
5. G. D. Reddy and P. Saggau, "Fast three-dimensional laser scanning scheme using acousto-optic deflectors," J. Biomed. Opt. **10,** (2005).
6. P. Bechtold, R. Hohenstein, and M. Schmidt, "Beam shaping and high-speed, cylinder-lens-free beam guiding using acousto-optical deflectors without additional compensation optics," Opt. Express **21,** 14627-14635 (2013).
7. W. Koechner, *Solid-State Laser Engineering* (Springer, 1996).
8. Y. Kremer, J. F. Leger, R. Lapole, N. Honnorat, Y. Candela, S. Dieudonne, and L. Bourdieu, "A spatio-temporally compensated acousto-optic scanner for two-photon microscopy providing large field of view," Opt. Express **16,** 10066-10076 (2008).
9. R. Salome, Y. Kremer, S. Dieudonne, J. F. Leger, O. Krichevsky, C. Wyart, D. Chatenay, and L. Bourdieu, "Ultrafast random-access scanning in two-photon microscopy using acousto-optic deflectors," J. Neurosci. Methods **154,** 161-174 (2006).
10. J. Schwiegerling, *Field Guide to Visual and Ophthalmic Optics* (SPIE Press, 2004).
11. O. Hernandez, M. Guillon, E. Papagiakoumou, and V. Emiliani, "Zero-order suppression for two-photon holographic excitation," Opt. Lett. **39,** 5953-5956 (2014).
12. N. Ji, D. E. Milkie, and E. Betzig, "Adaptive optics via pupil segmentation for high-resolution imaging in biological tissues," Nat. Methods **7,** 141-147 (2010).
13. N. Ji, T. R. Sato, and E. Betzig, "Characterization and adaptive optical correction of aberrations during in vivo imaging in the mouse cortex," Proc. Natl. Acad. Sci. U. S. A **109,** 22-27 (2012).
14. P. F. McManamon, P. J. Bos, M. J. Escuti, J. Heikenfeld, S. Serati, H. K. Xie, and E. A. Watson, "A Review of Phased Array Steering for Narrow-Band Electrooptical Systems," Proc. Ieee **97,** 1078-1096 (2009).

15. B. Apter, U. Efron, and E. Bahat-Treidel, "On the fringing-field effect in liquid-crystal beam-steering devices," Appl. Opt. **43,** 11-19 (2004).
16. W. Mittmann, D. J. Wallace, U. Czubayko, J. T. Herb, A. T. Schaefer, L. L. Looger, W. Denk, and J. N. Kerr, "Two-photon calcium imaging of evoked activity from L5 somatosensory neurons in vivo," Nat. Neurosci. **14,** 1089-1093 (2011).
17. P. Theer, M. T. Hasan, and W. Denk, "Two-photon imaging to a depth of 1000 microm in living brains by use of a Ti:Al2O3 regenerative amplifier," Opt. Lett. **28,** 1022-1024 (2003).
18. E. Beaurepaire, M. Oheim, and J. Mertz, "Ultra-deep two-photon fluorescence excitation in turbid media," Opt. Commun. **188,** 25-29 (2001).
19. G. Katona, G. Szalay, P. Maak, A. Kaszas, M. Veress, D. Hillier, B. Chiovini, E. S. Vizi, B. Roska, and B. Rozsa, "Fast two-photon in vivo imaging with three-dimensional random-access scanning in large tissue volumes," Nat. Methods **9,** 201-208 (2012).
20. P. A. Kirkby, K. M. Srinivas Nadella, and R. A. Silver, "A compact Acousto-Optic Lens for 2D and 3D femtosecond based 2-photon microscopy," Opt. Express **18,** 13721-13745 (2010).
21. G. D. Reddy, K. Kelleher, R. Fink, and P. Saggau, "Three-dimensional random access multiphoton microscopy for functional imaging of neuronal activity," Nat. Neurosci. **11,** 713-720 (2008).
22. F. Helmchen and W. Denk, "Deep tissue two-photon microscopy," Nat. Methods **2,** 932-940 (2005).
23. K. Svoboda and R. Yasuda, "Principles of two-photon excitation microscopy and its applications to neuroscience," Neuron **50,** 823-839 (2006).

1. Introduction

Spatial shaping of laser beams, by tailoring amplitude and phase of the light field, has major applications in applied optics, including material processing, laser displays, optical communication and microscopy. For high throughput these applications require the technical ability to control the beam shape at high temporal rate. Active phase shaping, often under fast feedback control, is achieved with a variety of technologies including deformable mirrors (DM) and liquid-crystal-based spatial light modulators (LC-SLM), which are either limited in speed to refresh rates of about 1 kHz (LC-SLM) or in the number of pixels in each dimension and thus in the number of discrete scan directions (fast DMs). Acousto-optic deflectors (AODs) [1], which are commonly used for beam steering in fast pointing devices, open the prospect for faster beam control with relatively large dynamic range. In standard use, AODs employ ultrasonic waves of constant frequency to establish a spatially homogeneous density grating in an acousto-optic crystal resulting in beam diffraction at an angle proportional to the acoustic frequency [2]. In principle, it should be possible to extend the application of AODs to generate arbitrary wavefront shapes by varying the spatial frequency of the density grating, and therefore the diffraction angle, along the active axis of the modulator. However, AOD-generated density gratings propagate with the velocity of sound in the crystal and thus fail to generate stationary beam profiles [3]. This issue has been worked around in the simple case of linearly chirped acoustic functions for the implementation of diffractive lenses. In this case, acoustic propagation produces angular scanning, which can be eliminated by adjunctive AODs fed with counter-propagating acoustic waves of the same chirp [4,5]. However, this method does not generalize to the case of acoustic waves carrying arbitrary non-linear frequency modulations. In the present work we propose to solve the non-stationarity issue by synchronizing a sub-nanosecond pulsed laser source to the refresh cycle of the acoustic wave following an earlier and similar proposal by Bechthold et al. [6]. In this configuration, the acousto-optic phase grating is reproduced to the same state each time the laser pulse crosses the AOD optical window, by repeating the same time-locked acoustic function from pulse to pulse [6]. The maximal AOD update rate is given by the time for an acoustic wave to sweep the AOD optical aperture and ranges from 10 kHz to over 200 kHz, depending on AOD aperture size and crystallographic parameters, faster than with any other existing technology.

AOD-based beam shaping may serve many applications demanding fast wavefront control. Notably, AOD update rates match the time scale of gain regeneration in high power laser pulse amplifiers [7]. AODs therefore offer the possibility to implement pulse-to-pulse shaping of amplified laser pulses with ultimate efficiency. In this paper we specifically envision femtosecond amplified laser pulse shaping for applications in non-linear microscopy

of bulk biological tissue. By permitting tilt and focus control of individual laser pulses, the modulator will allow addressing points within the accessible tissue volume at laser repetition rate. In the following, we derive the relationship between the acoustic wave pattern in the AOD and the spatial beam shape of the light diffracted from the AOD. As diffraction patterns in single AODs are one-dimensional, we elaborate the symmetry constraints applying to the representation of arbitrary two-dimensional phase functions and quantify the resulting approximation errors using the Zernike polynomial expansion. We demonstrate experimentally the beam shaping capability of this system and characterize its performance in terms of resolution and phase accuracy.

2. Methods

2.1 Experimental layout

2.1.1 Optical setup

We set up a system [Fig. 1] consisting of two AODs (DTS.XY.400, L = 6.7 mm active aperture, 800-1000 nm, 45 mrad deflection range, 35 MHz acoustic bandwidth at 800 nm, AA Optoelectronic, Orsay, France) for beam diffraction in perpendicular directions (referred to as X-AOD and Y-AOD) together with a third AO crystal (AA.MTS.141, L = 4.5 mm active aperture, 840 nm, AA Optoelectronic) for compensation of spatial and temporal dispersion (referred to as AOM) [8]. By construction, X- and Y-AODs featured collinear direction of the incident beam and the first order diffracted beam at the central acoustic frequency. The access time of the AODs is $t_{access} = L/v$ = 10.3 µs, with v = 650 m/s as acoustic velocity for anisotropic, non-rotated diffraction in TeO_2.

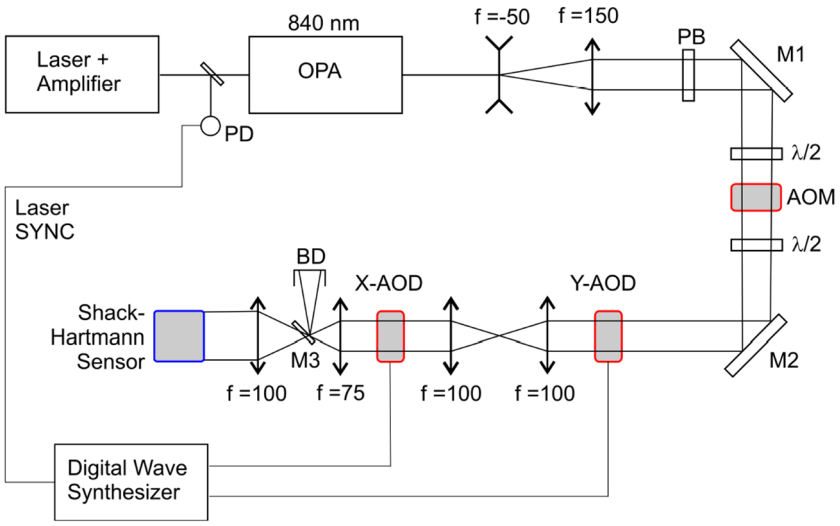

Fig. 1. Optical setup. The laser output (200 fs pulses, 840 nm, 80 kHz repetition) was magnified by a first telescope to fit the aperture of the acousto-optic elements. A long pass filter (PB) blocked residual OPA pump light and the linear polarization was adjusted at the entrances of the AOM and the Y-AOD using half-wave plates. A second telescope imaged the Y-AOD onto the X-AOD and the resulting wavefront was analysed with a Shack-Hartmann sensor after passing through a third telescope with a 4/3 magnification and after pulse power adjustment by dispersing excess power in a beam dump (BD). Y-AOD, X-AOD and Shack-Hartmann sensor were placed in optically conjugated planes. The position of the AOM with respect to the Y-AOD was adjusted to compensate for the temporal dispersion of the acousto-optic elements. The output of a fast photodiode (PD) served to synchronize the AOD update to the laser emission.

As light source we used a laser system (Pharos SP6, Light Conversion, Vilnius, Lithuania) consisting of a diode-pumped Yb:KGW mode-locked oscillator (1028 nm emission, 76 MHz repetition, 90 fs pulse duration, 1 W power) together with a diode-pumped

Yb:KGW chirped-pulse amplifier (80 kHz repetition, 190 fs duration, 75 µJ pulse energy, 6 W power). The amplified pulses were parametrically converted in an optical parametric amplifier (630-2600 nm tuning range, Orpheus OPA, Light Conversion) set to 840 nm and using about 20% of 500 mW available output power. Residual pump light (514 nm) from the OPA was suppressed with a longpass filter (750 nm cut-on, Thorlabs). The laser beam was magnified to fill the AOM aperture and the beam polarization at the AOM and the Y-AOD entrance were optimized using achromatic half-wave plates (690-1200 nm, Thorlabs). Y-AOD and X-AOD were conjugated by an afocal telescope with a magnification of one. The AOM to Y-AOD distance was adjusted to compensate for the pulse temporal dispersion in the acousto-optic systems using a GRENOUILLE autocorrelator (Swamp Optics) and the AOM frequency was set to compensate for the spatial dispersion of the laser pulse in the AODs [8,9]. Finally, the output wavefront was recorded using a Shack-Hartman sensor (HASO 4 FIRST, 3.6x4.6 mm aperture, 32x40 micro lenses, λ/100 accuracy, Imagine Optic, Orsay, France) conjugated to the AODs by a second telescope with magnification of 1, 4/3 or 10, using 100 mm/100 mm, 75 mm/100 mm (as shown in Fig. 1) or 50 mm/500 mm lens tandems, respectively.

2.1.2 Generation of the signals controlling the AODs

The radio frequency signals feeding the two AODs were obtained from a two channel direct digital synthesizer (DDS) with integrated power amplifier and digital input interface (DDSPA, AA Optoelectronic) receiving digital command inputs from two 50 MHz digital I/O boards (NI PXIe 6537, National Instruments). The digital commands comprised 32 bits coding for the acoustic frequency (23 bit) and acoustic power (8 bit). Synchronization of the AOD writing cycle to the laser emission was established as follows. First, an 80 kHz laser synchronisation signal was generated with a Schmitt trigger (74VHC123A, Fairchild Semiconductors) from the output of a fast photodiode at the exit of the Pharos pulse compressor. This timing signal was then used to trigger two digital pulse train generators on a multiple timer/counter board (NI PXIe-6612, National Instruments) providing synchronous clock signals for pixel update to the digital I/O and DDS circuits, respectively, in response to single trigger events. The clock signals consisted of 14 MHz trains of 145 pulses, commensurable with the given access time of the AODs (10.3 µs, see above), comprising a programmable post-trigger delay, common to both clocks, and a fixed phase shift to optimize the relative timing of I/O and DDS functions. The AOD update process was configured under LABVIEW 2015 (National Instruments) by supplying the I/O boards, through direct memory access, with update values of acoustic frequency and power, pre-calculated for every cycle of the write clock. The post-trigger delay was experimentally adjusted to shape the following pulse in such a way that the diffracted wavefront was well centred to the optical axis.

2.1.3 Optical wavefront analysis

For the analysis of single pulse wavefronts, we synchronized the image capture of the Shack-Hartmann sensor to the laser sync and set the AOD acoustic power to zero for all pulses emitted within the integration time of the camera, except for one pulse. The integration time was set to its minimum (500 µs). To meet the dynamic range of the Shack-Hartmann sensor, the pulse power was attenuated by passing the focalized beam through a 45° dielectric mirror with optical grade rear surface (~99% reflectance 750-1100 nm, BB1-E03P, Thorlabs). Optical wavefronts were reconstructed from the measured wavefront slopes using HASO 3.1 software (Imagine Optic) together with a custom plug-in for processing of large datasets (kindly provided by Imagine Optic) and exported to MATLAB 2013 (Mathworks).

2.2 Phase and amplitude modulation by a single AOD

Let us first consider a single AOD providing phase and amplitude modulation along the x-axis and an incident beam propagating along the z-axis. The beam has a given incident amplitude profile $A_{in}(x,y)$, as e.g. uniform or Gaussian, and a given incident wavefront $\varphi_0(x,y)$; thus:

$A_{in}(x,y,z) = A_{in}(x,y)e^{i(k_0 z+\varphi_0(x,y))}$, where k_o is the wave vector of the incident pulse. At the time of arrival of the laser pulse, the AOD is filled with an ultrasonic pattern of frequency $f_{AOD}(x)$ and amplitude $a_{AOD}(x)$ at a position x in the AOD, with $x = 0$ at the beam centre. Hereby it is implicitly assumed that the laser pulse is sufficiently short so that propagation and hence time dependence of the ultrasonic pattern are negligible during the diffraction process. Amplitude and frequency modulation is generated by time-varying command signals for frequency and power, $f(t)$ and $a(t)$, respectively, applied to the transducer. The time when the commands have to be active to set the frequency and power at position x is $t = x/v$, with v, the acoustic wave velocity (typically 650 m/s for TeO_2 in shear mode), and with the time origin $t = 0$ chosen as the time when the command for position $x = 0$ is applied, thus $f_{AOD}(x) = f(x/v)$ and $a_{AOD}(x) = a(x/v)$.

Therefore, after interaction with the AOD, the wavefront $A_{out}(x,y,z)$ is given by: $A_{out}(x,y,z) = A_{in}(x,y)\ T\left(a_{AOD}(x)\right)\ e^{i(k_0 z+\varphi_0(x,y)+\varphi_{AOD}(x))}$, where T is the characteristic amplitude transfer function of the AOD, expressing the fraction of the input light transferred into the first diffraction order, as function of the acoustic wave amplitude a_{AOD}. The AOD provides therefore a complex spatial modulation $M_{AOD}(x)$ given by:

$$M_{AOD}(x) = T\left(a_{AOD}(x)\right)\ e^{i\varphi_{AOD}(x)} \tag{1}$$

consisting of an amplitude modulation $T(a_{AOD}(x))$, which is an implicit function of the amplitude modulation of the acoustic wave $a_{AOD}(x)$, and a phase modulation $\varphi_{AOD}(x)$, which is related to the frequency modulation $f_{AOD}(x)$ in a more complex way.

At each point x of the AOD, the rays are deflected by an angle $\theta(x)$ given by twice the Bragg angle:

$$\theta(x) = \frac{\lambda f_{AOD}(x)}{v} \tag{2}$$

At any point x, the rays leaving the AOD are perpendicular to the wavefront. Therefore, the optical path difference between the position x and $x+dx$ of the wavefront due to the deflection angle $\theta(x)$ is $\theta(x)dx$ and the wavefront is related to the acoustic frequency by:

$$\frac{d\varphi_{AOD}(x)}{dx} = \frac{2\pi}{\lambda}\theta(x) = \frac{2\pi f_{AOD}(x)}{v} \tag{3}$$

Integration gives:

$$\varphi_{AOD}(x) = \frac{2\pi}{v}\int_{-L/2}^{x} f_{AOD}(u)\,du \tag{4}$$

by choosing the position of edge of the AOD optical aperture at $x = -L/2$ as reference position for the optical phase, where L is the aperture size, and further assuming that the beam is aligned to the crystal centre. This expression shows that the phase profile created at a position x does not only depend on the ultrasonic frequency at the pixel x in the AOD, but non-locally on the entire ultrasonic frequency pattern from the reference position to the point x. Eq. (4) can be rewritten as:

$$\varphi_{AOD}(x) = \frac{2\pi}{v}\left(x\ f_{AOD}(x) - \int_{-L/2}^{x} u\frac{df_{AOD}}{du}du + L/2\ f_{AOD}(-L/2)\right) \tag{5}$$

Eq. (5) shows that the wavefront differs from the local term $\frac{2\pi}{v}\left(xf_{AOD}(x)\right)$ due to all changes in frequency $\left(u\frac{df_{AOD}}{du} \neq 0\right)$ between the reference and the x position. Eq. (4) allows

reconstruction of the output wavefront knowing the applied frequency function, while Eq. (3) allows determining the frequency pattern corresponding to a target wavefront $\varphi_{AOD}(x)$. In the case of a digital wave synthesizer the functions $f(x)$ and $a(x)$ are discretized with a step size set by the pixel writing clock. If the acoustic frequency is changed at N positions x_i, for $i = 1$ to N, the frequencies f_i to be applied between x_i and x_{i+1} to create a target wavefront $\varphi_{AOD}(x)$ are:

$$f_{AOD}(x_i) = \frac{v}{2\pi} \frac{\varphi_{AOD}(x_{i+1}) - \varphi_{AOD}(x_i)}{x_{i+1} - x_i}, \text{ for } i = 1 \text{ to } N-1 \tag{6}$$

Conversely, a series of frequencies f_i ($i = 1$ to N) will create a wavefront $\varphi_{AOD}(x)$ given by:

$$\varphi_{AOD}(x_{i+1}) = \varphi_{AOD}(x_i) + \frac{2\pi}{v}(x_{i+1} - x_i)\ f_{AOD}(x_i), \text{ for } i = 1 \text{ to } N-1 \tag{7}$$

2.3 Accuracy of wavefront control

In Eq. (5) and Eq. (7) it is implicitly assumed that a given frequency f_i is valid exactly between position x_i (equivalent to the time x_i/v) and x_{i+1} (equivalent to the time x_{i+1}/v). A random jitter of standard deviation (STD) $\Delta\tau$ in the electronic control of the AOD frequency pattern (see Discussion) induces a corresponding random phase jitter $\Delta\varphi_{AOD}$ at each frequency step Δf [see Fig. 2(a)]. A single frequency step Δf causes an angular deflection of $\Delta\theta = \lambda\Delta f/v$ of the wavefront, and a temporal jitter $\Delta\tau$ translates to a spatial jitter $\Delta x = v\Delta\tau$ in the location of the phase change. The resulting phase jitter $\Delta\varphi_{AOD}$ is given by $\Delta\varphi_{AOD} = (2\pi/\lambda)\Delta x\ \Delta\theta$ and thus:

$$\Delta\varphi_{AOD} = 2\pi\ \Delta\tau\ \Delta f \tag{8}$$

In case of a wavefront generated from N identical frequency steps, corresponding to a linear frequency chirp, the phase jitter will accumulate in a manner analogous to a one-dimensional random walk of constant step size to a standard deviation of $\sqrt{N}\ \Delta\varphi_{AOD}$, which indicates the maximal phase error to be expected in AOD-shaped single pulse quadratic wavefronts.

2.4 Phase and amplitude modulation by two orthogonal AODs

2D wavefront shaping can be achieved using two perpendicularly crossed AODs. This configuration will create 2D phase and amplitude modulation according to:

$$M_{AOD}(x,y) = T_1(a_1(x))\ T_2(a_2(y))\ e^{i(\varphi_1(x)+\varphi_2(y))} \tag{9}$$

where $a_1(x)$ and $a_2(y)$ are the ultrasonic amplitudes, T_1 and T_2 the AOD transfer functions, and $\varphi_1(x)$ and $\varphi_2(y)$ the phase functions in the X-AOD and Y-AOD, respectively, in analogy to Eq. (3). It follows that two-dimensional phase functions $\varphi(x,y)$ can be fully reproduced in the crossed AOD configuration if they are linearly separable, namely obeying $\varphi(x,y) = \varphi_1(x)+\varphi_2(y)$, while functions containing non-separable terms, like crossed polynomial terms of the form $x^a y^b$, can only be approximately realized. Functions containing only non-separable terms cannot be realized with two orthogonal AODs.

2.5 Diffractive lenses

Wavefront quadratic curvature corresponding to the effect of a spherical lens has the analytical form $\varphi(x,y) = \frac{2\pi}{\lambda}\frac{(x^2+y^2)}{2F}$, where F is the effective focal length of the lens, which is linearly separable into $\varphi_1(x) = \frac{2\pi}{\lambda}\frac{x^2}{2F}$ and $\varphi_2(y) = \frac{2\pi}{\lambda}\frac{y^2}{2F}$. Spherical lenses are therefore represented without error by an orthogonal XY-AOD pair. Using Eq. (3), and considering only the X-AOD, it follows that $\varphi_1(x)$ is generated by linearly-chirped frequency signal

$f_1(x) = \frac{v}{\lambda}\frac{x}{F_{AOD}}$ applied to the X-AOD. Recalling than $t = x/v$, and defining the chirp rate as $\alpha = \Delta f / \Delta t$, the effective focal length F_{AOD} can be expressed as:

$$F_{AOD} = \frac{v^2}{\lambda\alpha} \tag{10}$$

Hence, AOD-generated diffraction lenses have a focal distance proportional to the reciprocal chirp rate.

2.6 Zernike Modes

Zernike modes often achieve fast convergence in the expansion series of complex optical wavefronts and therefore are a convenient means of assessing beam shaping properties. The Cartesian representation of the Zernike polynomials [10] immediately reveals the decomposition into linearly separable and non-separable polynomial terms. Of the fourteen first modes, five modes are completely reproducible in the XY-AOD configuration, six modes are partially reproducible, while three are not reproducible, see Table 1.

Table 1. Decomposition of the wavefront generated in the XY-AOD configuration in Zernike modes up to 4th order in Cartesian coordinates. Error and predicted match index are as defined in Eq. (11). The functions are indexed according to either radial (subscript) and azimuthal (superscript) order, or the composite Noll index. φ_1 and φ_2 are phase functions of X- and Y-AOD, respectively, as defined in Eq. (9).

Aberration		Noll	Zernike Polynomials	AOD approx.	Error	Match
Tilt	Z_1^{-1}	1	$2Y$	$\varphi_1 = 0;\ \varphi_2 = 2Y$	0	1
Tip	Z_1^{1}	2	$2X$	$\varphi_1 = 2X;\ \varphi_2 = 0$	0	1
Oblique Astig.	Z_2^{-2}	3	$\sqrt{6}2XY$	$\varphi_1 = 0;\ \varphi_2 = 0$	$2\sqrt{6}XY$	0
Defocus	Z_2^{0}	4	$\sqrt{3}\left(2X^2+2Y^2-1\right)$	$\varphi_1 = \sqrt{3}2X^2 - 1;$ $\varphi_2 = \sqrt{3}2Y^2$	0	1
Vertical Astig.	Z_2^{2}	5	$\sqrt{6}\left(X^2-Y^2\right)$	$\varphi_1 = \sqrt{6}X^2;\ \varphi_2 = -\sqrt{6}Y^2$	0	1
Vertical Trefoil	Z_3^{-3}	6	$\sqrt{8}\left(3X^2Y-Y^3\right)$	$\varphi_1 = 0;\ \varphi_2 = -\sqrt{8}Y^3$	$6\sqrt{2}X^2Y$	0.32
Vertical Coma	Z_3^{-1}	7	$\sqrt{8}\left(3X^2Y+3Y^3-2Y\right)$	$\varphi_1 = 0;\ \varphi_2 = 3Y^3 - 2Y$	$6\sqrt{2}X^2Y$	0.59
Horizontal Coma	Z_3^{1}	8	$\sqrt{8}\left(3X^3+3XY^2-2X\right)$	$\varphi_1 = 3X^3 - 2X;\ \varphi_2 = 0$	$6\sqrt{2}XY^2$	0.59
Oblique Trefoil	Z_3^{3}	9	$\sqrt{8}\left(X^3-3XY^2\right)$	$\varphi_1 = X^3;\ \varphi_2 = 0$	$-6\sqrt{2}X^2Y$	0.32
Oblique Quadrafoil	Z_4^{-4}	10	$\sqrt{10}\left(4X^3Y-4XY^3\right)$	$\varphi_1 = 0;\ \varphi_2 = 0$	Z_4^{-4}	0
Oblique 2nd Astigm.	Z_4^{-2}	11	$\sqrt{10}\left(8X^3Y+8XY^3-6XY\right)$	$\varphi_1 = 0;\ \varphi_2 = 0$	Z_4^{-2}	0
1st Spherical Aberr.	Z_4^{0}	12	$\sqrt{5}\left(6X^4+12X^2Y^2+$ $6Y^4-6X^2-6Y^2+1\right)$	$\varphi_1 = \sqrt{5}\left(6X^4-6X^2+1\right);$ $\varphi_2 = \sqrt{5}\left(6Y^4+1\right)$	$12\sqrt{5}X^2Y^2$	0.46
Vertical 2nd Astigm.	Z_4^{2}	13	$\sqrt{10}\left(4X^4-4Y^4$ $-3X^2+3Y^2\right)$	$\varphi_1 = \sqrt{10}(4X^4-3X^2);$ $\varphi_2 = \sqrt{10}\left(-4Y^4+3Y^2\right)$	0	1
Vertical Quadrafoil	Z_4^{4}	14	$\sqrt{10}\left(X^4-6X^2Y^2+Y^4\right)$	$\varphi_1 = \sqrt{10}X^4;\ \varphi_2 = \sqrt{10}Y^4$	$6\sqrt{10}X^2Y^2$	0.33

The approximation error is given by the deviation of the AOD-approximated wavefront Z_i^{AOD} with respect to the corresponding Zernike template mode Z_i (with i, the composite Noll index). In our analysis we quantify this error by the RMS score of the relevant coefficient in the expansion series of Z_i^{AOD}:

$$m(i) = \sqrt{a_{ii}^2 \Big/ \left(\sum_{j=1}^{j=35} a_{ij}^2 \right)} \tag{11}$$

with a_{ij}, the coefficients of the Zernike expansion (to the 35th Noll order) of Z_i^{AOD}, that is $Z_i^{AOD}(x,y) = \sum_{j=0}^{j=35} a_{ij}\ Z_j(x,y)$, giving values between zero (no match) and one (perfect match).

3. Results

To evaluate the beam shaping capability of the AODs in the synchronized mode, we set up a beam shaper consisting of an XY pair of AODs in 4f configuration and a third acousto-optic element (AOM) for compensation of chromatic and temporal dispersion [8]. We measured the spatial phase of single laser beam pulses after interaction with the acousto-optic phase gratings in the AODs using a Shack-Hartmann phase sensitive camera positioned in an optical plane conjugated to the AODs, as illustrated in Fig. 1. By programming different types of acoustic grating functions we verify the operation of the proposed AOD beam shaper.

3.1 Timing accuracy

Laser and acoustic wave generation involve complex electronic circuits, including proprietary electronics with incomplete timing specifications as well as digital circuits running on asynchronous clocks, altogether challenging synchronization accuracy. We therefore set out to assess the timing properties of the system by characterizing directly the pulse-to-pulse phase variability present in the wavefronts after diffraction in the AODs. For this we defined a simple test protocol, schematized in Fig. 2(a), consisting of a single acoustic frequency jump applied to the Y-AOD producing a roof-shaped planar waveform in the y-direction [Fig. 2(a)]. We determined the statistics of the y-position of the wavefront deflection using single-pulse phase detection as explained in Methods. The centroid of the deflection can be attributed to the extrapolated intersection point of the two emerging planar wavefronts with a spatial precision much higher than defined by the Shack-Hartmann microlens distance. The standard deviation Δy of the intersection point is a direct measure of the temporal jitter $\Delta t = \Delta y/v$, with v the acoustic velocity, and of the resulting phase jitter $\Delta\varphi_{AOD}$, according to Eq. (8) and Fig. 2(a). Fig. 2(b) depicts the fitted wavefronts of 20 pulses (out of 1000 measured) together with the mean phase in response to 10 MHz acoustic step amplitude. Because the only deflection applied was in y-direction the one-dimensional wavefronts in Fig. 2(b) involved averaging of the phase in x-direction. In this way we measured a space jitter Δy of 5.5 μm, a temporal jitter $\Delta\tau$ of 8.7 ns and a phase jitter $\Delta\varphi_{AOD}$ of $2\pi/10$ rad (*i.e.* 0.1λ) [Fig. 2(c)], representing STD. We performed the same measurement for various step amplitudes between -10 and +10 MHz [Figs. 2(d) and 2(e)] confirming that space and time jitters are independent of the magnitude of frequency changes applied during digital synthesis of the acoustic wave [Fig. 2(f)]. This jitter is much smaller than the clock period T_{write} used to write the acoustic wave (T_{write} = 71 ns for a 14 MHz clock) and therefore does not produce significant crosstalk between neighbouring pixels during acoustic wave synthesis.

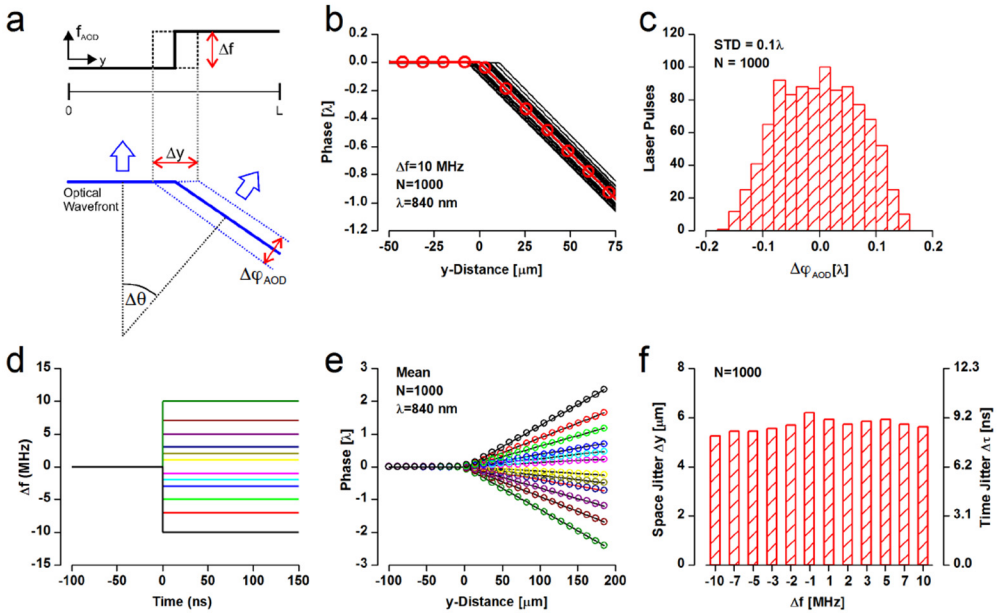

Fig. 2. Accuracy of AOD wavefront control. a) Schematic of the test protocol consisting of an acoustic frequency step applied to the Y-AOD. A temporal jitter Δτ in the control of the ultrasonic wave results in a spatial jitter $\Delta y = v\Delta\tau$ in the transition centroid of the wavefront following a stepped frequency command, which in turns causes a phase jitter $\Delta\varphi_{AOD}$. b) Measured wavefronts obtained from a 10 MHz frequency step: overlay of 20 individual wavefronts (black) and mean wavefront (red; N=1000) obtained from linear fits to the reconstructed wavefronts of single laser pulses. Circles (red) indicate the lineup of microlenses in y direction. Phase is set to zero at the position of the mean transition centroid defined as the zero position ($y = 0$). c) Histogram of the measured phases for N=1000 laser pulses with respect to the mean phase. d-f) Summary of phase measurements as in a), but for different amplitudes of frequency step Δf (d). e) Measured mean phases with microlens positions as circles. f) Spatial and temporal jitters, Δy and $\Delta\tau$, respectively, as a function of the frequency step amplitude, evaluated from the standard deviation of the respective phase histograms as shown in (c).

3.2 Stable diffractive lenses

Given accurate timing stability we expect the system to produce stable diffractive lenses for jitter-free optical wave defocus. According to Eq. (3) wavefronts of quadratic curvature (Zernike defocus, Table 1) are created from linearly-chirped acoustic gratings (see Methods). To test the defocus we first applied a series of chirped frequency signals with chirp rates between -1.5 and +1.5 MHz/μs to the Y-AOD [Fig. 3(a)] and measured the resulting wavefronts as before [Fig. 3(b)]. The measured phase was indeed well fitted by parabolic functions [Fig. 3(b)].

The effective focal length calculated from the phase curvature was a linear function of the inverse chirp rate [Fig. 3(c)] in agreement with Eq. (10), exhibiting a slope of 59.2 +/-0.5 cm/(μs/MHz) slightly larger than the theoretical calibration of an ideal Bragg lens of 50.3 cm/(μs/MHz) at 840 nm as given by Eq. (10). Since AOD diffraction gratings are one-dimensional, single AOD-generated lenses are cylindrical. However, since spherical lenses are equivalent to crossed cylindrical lenses of same focal length, spherical diffraction lenses are obtained by feeding synchronously the same acoustic chirp to X- and Y-AOD [Fig. 3(d)]. For the creation of quadratic wavefronts we expect an accumulated phase error of $2\pi\sqrt{N}\,\Delta\tau\Delta f$ with N, the pixel number, $\Delta\tau$, the synchronization jitter, and Δf, the acoustic frequency change per pixel (see Methods). Since Δf is limited by the available acoustic bandwith f_{BW} to $\Delta f = f_{BW}/N$, the upper limit of the phase error is $2\pi f_{BW}\Delta\tau/\sqrt{N}$ in quadratic wavefronts. Thus, with $\Delta\tau$ = 8.7 ns [Fig. 2(f)], f_{BW} = 35 MHz (see Methods) and N = 75, corresponding to the

detection pupil in Fig. 3(b), the maximum error expected amounts to 0.035λ. Notably, this error is of the same order of magnitude as the error of phase reconstruction in our phase measurement (see Methods). In fact, we find similar variance in our data of linear (N = 1) and quadratic wavefronts (N = 75). Therefore, within the limits of our measurement, and for practical considerations, phase error due to accumulation of synchronization noise is negligible small.

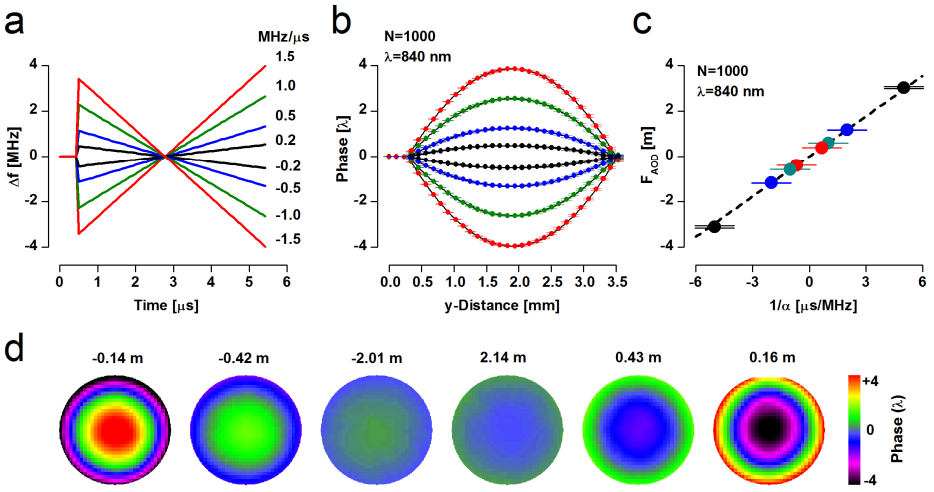

Fig. 3. AOD-generated diffractive lenses. a)-c) Cylindrical lenses created within a 3.6 mm diameter optical pupil by linearly chirped acoustic waves applied to the Y-AOD. Shown are the acoustic frequency signals (a) with chirp rates between -1.5 and +1.5 MHz/µs, the mean wavefronts (with vertical error bars indicating STD) obtained from N = 1000 single-pulse phase measurements (b, circles; color-coded for different chirp rates) and parabolic fits to the data (straight lines; black) and the focal distances (c) calculated from fitted wavefronts as function of the inverse chirp rate together with the line (dashed) of linear regression. Phases are set to zero at the edge of the pupil (y=0). Chirped acoustic waves filling the pupil involved 75 discrete frequency update steps. d) Concave and convex spherical lenses created by applying the same chirped acoustic signal to X- and Y-AOD. The panel shows two-dimensional phase images of a detection pupil of 2.7 mm (in AOD coordinates) encompassing 58 generation steps of the acoustic waveforms after averaging about 100 pulses. Numbers on top are the focal distances calculated from the wavefront curvatures.

3.3 Zernike Modes

The limitations of AODs to approximate arbitrary wavefronts stem from the condition that the generating functions must be linearly separable in orthogonal Cartesian coordinates. To elucidate the implications of symmetry constraint we measured the wavefronts of functions approximating Zernike polynomials up to 4th order using the decomposition given in Table 1.

We find good agreement between measured and predicted phase functions [Fig. 4(a)] and associated match indices [Fig. 4(b)]. Thus, tilts (i = 1, 2; m = 1), focus (i = 4; m = 1), and 0° astigmatism (i = 5, 13; m = 0.98) are completely reproduced, while trefoil (i = 6, 9; m = 0.3), coma (i = 7, 8; m = 0.6) and spherical aberration (i = 12; m = 0.46) are partially reproduced. 45° astigmatism (i = 3, 11) and quadrafoil (i = 10), on the other hand, yield zero match. As expected (see Table 1) symmetry cuts significantly on the representation of higher order modes. In principal, however, it is possible to enhance the representation of individual modes by rotation of the wavefront (or the AOD coordinate system) at the expense of modes of same radial, but different azimuthal order. For instance, 45° rotation obviously transforms 45°-astigmatism (m = 0) into 0°-astigmatism (m = 1) and vice versa. This suggests that better representation of higher order modes could be achieved by independent modulation in diagonal directions by addition of two AODs as described below (see Discussion).

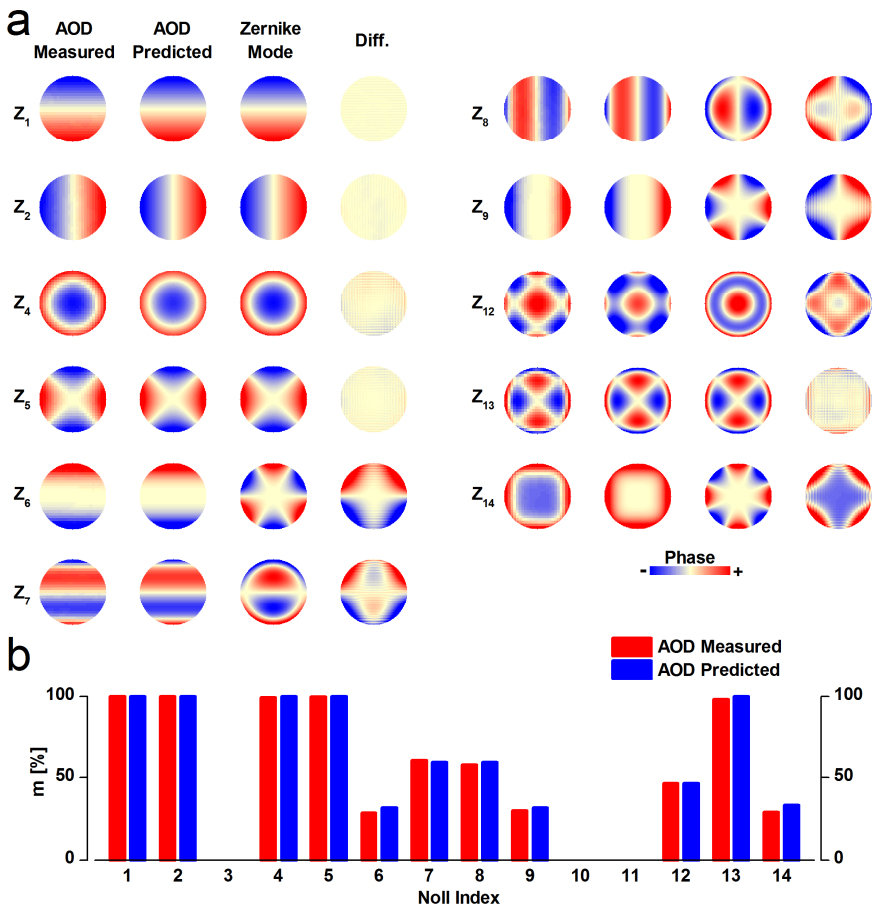

Fig. 4. Approximation of Zernike polynomial phase functions. a) Measured 2D spatial phase of the laser beam diffracted by the X-Y AODs for approximation of Zernike polynomial functions of Noll index up to 14 (first column), shown together with the expected phase (second column), the Zernike template (third column) and the difference between measured phase and template phase (pointwise difference; forth column). The pupil size was 2.7 mm corresponding to 58 discretization steps of the acoustic waveform. Phases in columns 1 to 3 are normalized to an RMS sum of unity. First and second order 45° astigmatisms (i = 3, 11) and quadrafoil (i = 10) are not reproduced in the AODs and therefore omitted. b) Measured (red) and predicted (blue; see Table 1) match index m [as defined by Eq. (11)] for Zernike modes to 4th order.

3.4 Astigmatism compensation

To illustrate the possibility of AOD-implemented adaptive correction of aberrant wavefronts we created virtual astigmatism by adding 0° astigmatism as an offset to the phase detector [Fig. 5(a)]. As vertical astigmatism corresponds to wavefronts with quadratic curvature of same magnitude, but opposite sign, in orthogonal directions, it is completely generated in the XY-AOD configuration as seen in Fig. 4(a). Thus, by supplying the AODs with linear chirps producing astigmatisms opposite to the astigmatism stored in the detector [Fig. 5(b)] it is possible to minimize the overall RMS deviation of the order of λ in the example given [Figs. 5 (c)-5(e)], and recover a nearly flat phase with λ/10 residual deviation [Fig. 5(d)].

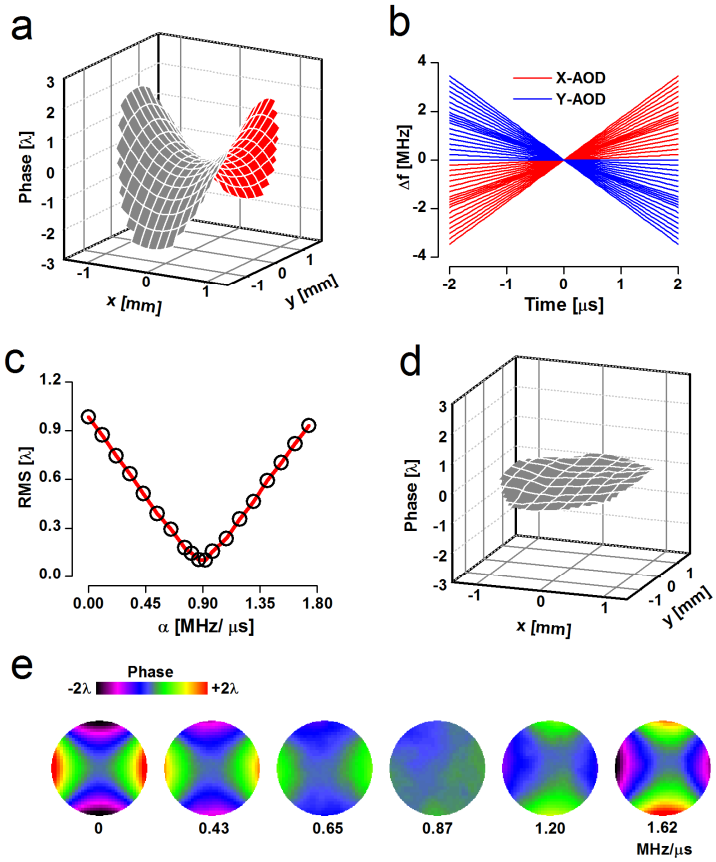

Fig. 5. Astigmatism compensation. An astigmatic wavefront is imposed as an offset pattern to the wavefront sensor. a) Output of the wavefront sensor at zero AOD compensation showing the astigmatism offset. b) Family of pairwise acoustic frequency signals fed to the X-AOD (red) and Y-AOD (blue) for different degrees of astigmatism compensation. Simultaneously applied chirps in X-AOD and Y-AOD had opposite sign, but same magnitude. c) Measured RMS values (RMS pixel sum measuring deviation from a flat waveform) as function of the applied compensating chirp for the acoustic frequency signals shown in b). d) Output of the wavefront sensor at optimal compensation. e) Beam 2D spatial phase at different levels of compensation with applied chirps given below. The measurements were performed on a 2.7 mm pupil (in AOD equivalent coordinates) enclosing 58 discrete synthetizing steps of the acoustic waveform.

4. Discussion

We have shown that AODs can perform optical phase modulation of pulsed laser beams with refresh rates close to 100 kHz, which is at least 2 orders of magnitude faster than achievable with current generation LC-SLMs. This performance is achieved using a pulse duration shorter than the period of the acoustic carrier wave (about <10 ns), satisfied by most pulsed lasers, and a pulse rate below the AOD repetition rate (97 kHz in our case) to permit shot-to-shot update of the acousto-optic phase grating. The use of smaller AODs or of faster propagating acoustic modes could adapt the AOD repetition rate to higher frequency lasers, but at the cost of fewer pixels. On the other hand, larger AODs like the 15 mm aperture devices used by Kremer et al. [8], which provide an access time of 23 μs, would yield a resolution of 323 pixels in combination with a 14 MHz update clock (as compared to 145 pixels in our case) at a repetition rate of 43 kHz, still much higher than alternative modulation methods.

AODs handle high-frequency components of the Fourier plane (large deflection angles) directly through the acousto-optic interaction induced by radio-frequency acoustic carrier gratings. By adding low frequency modulation to the carrier wave, AODs allow shaping of localized optical point spread functions while scanning large deflection angles, a combination essential for most applications like two-photon microscopy. In addition to speed, AOD-SLMs, as proposed in this work, offer large angular separation of first and zero order beams (> 9° in our case) and the capability to control the spatial distribution of the beam intensity at the same time, and with same spatial resolution, as its phase. LC-SLMs, in contrast, are pure phase modulators and require immense efforts to clear the modulated beam from un-diffracted zero order light appearing at the centre of the optical axis and forming a high intensity spot in the centre of the Fourier plane, e.g. the focal plane of a microscope objective [11].

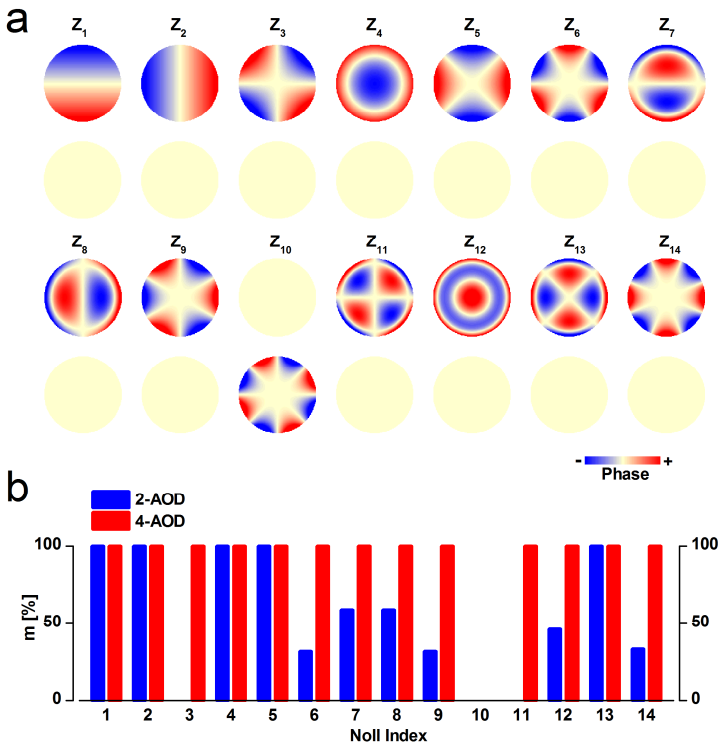

Fig. 6. Representation of Zernike phase functions in the four-AOD configuration. a) Predicted representation of Zernike modes up to Noll index 14 when shaped by four AODs with active axes oriented 0°, 45°, 90°, 135°. Shown are the normalized phases together with the deviation (pointwise difference) from the Zernike mode of same order, with Z_{12} being the 1st order spherical aberration. The predictions are based on decomposition of Zernike functions into compatible polynomial terms analogous to Table 1. b) Predicted match index of Zernike modes shaped in the 4 AOD (red) versus the 2 AOD configuration (blue).

While LC-SLMs are true two-dimensional phase modulators, the AOD-implementation equals two one-dimensional modulators in series. In consequence, the total number of pixels in the AOD configuration is the sum of x- and y-pixels versus the product in the case of LC-SLM. This restricts the symmetry of phase patterns that can be reproduced in the AOD-SLM, as we demonstrated in the case of the Zernike modes. These constraints, however, can be more or less limiting depending on the application. 3D focus control relies exclusively on tilt and defocus and therefore is fully achieved in AOD beam shaping mode. Furthermore, in adaptive optics experiments of complex tissue imaging it is often found that local corrections of low order, e.g. tilt, performed on a segmented pupil perform better than global corrections

of high order applied to the entire pupil [12,13]. Although AOD-SLMs do not allow segmentation into arbitrary independent sub-pupils as achieved in LC-SLMs, they might still provide useful approximations for segmented phase correction. In this context it is interesting to note that in practice LC-SLM corrections are preferentially performed on overlapping rather than independent sub-pupils in order to increase the signals used for iterative optimization [12]. Moreover, if higher order modes, like primary spherical aberration for instance, are to be fully corrected at high speed one could set up an AOD system comprising more than two AODs. A configuration composed of four AODs, with their active axis separated by 45°, provides an accurate representation of wavefronts separable into directions x, y, $x+y$ and $x-y$, instead of only directions x and y in the 2-AOD configuration. We expect the 4-AOD configuration to achieve full representation ($m = 1$) of all modes listed in Table 1 including primary spherical aberration ($i = 12$) with the only exception of oblique quadrafoil ($i = 10$) [Figs. 6(a)-6(b)].

Another distinct, and so far neglected [6], aspect of AOD-based systems is that pixels are not independent, as in the LC-SLM, but relate to other pixels through the non-local relationship given in Eq. (4). AODs modulate the optical phase in a fundamentally non-local mode which has important implications. First, pixels can inherit noise from preceding pixels (although these pixels are written later in time, see Methods). We therefore consider it an important outcome of our study to show that synchronization noise can be minimized to a level that the accumulated phase error caused by jitter-induced pixel noise remains actually very small. With regard to the origin of the residual synchronization jitter of about 10 ns in our system we believe that it is dominantly produced by the acoustic wave synthesizer and reflects the asynchrony of the pixel write clock with respect to the phase of the acoustic wave. In our system we use an acoustic carrier frequency of 95 MHz corresponding to an acoustic phase period of 10 ns, in the order of the observed synchronization jitter. A second implication of non-locality is that the AOD-generated phase is always continuous, even though acoustic frequencies are discretized, and free of 2π phase resets. This is a notable difference to LC-SLMs. Therefore AODs are not liable to efficiency loss in the same way as LC-SLMs. In LC-SLMs one major mechanism of efficiency loss, and hence diffraction ghosts, is due to the effective low-pass filtering of the phase reset discontinuity by fringing inter-electrode electric fields [14,15]. In consequence, aberrant diffraction intensity emerges within the angular scanning range of LC-SLMs as function of the phase reset period and therefore principally increases at larger diffraction angles [15]. In AODs, on the other hand, efficiency losses are incurred by aberration of the acoustic waveform in the near field of the piezoelectric wave generator causing deviation from Bragg diffraction [1]. In AODs, therefore, aberrant diffraction originates mostly from off-centre regions and with lesser dependence on diffraction angle.

AOD pulse shaping may offer novel perspectives for non-linear microscopy. Although the AOD update rate is orders of magnitude lower than the repetition rate of standard laser oscillators (80 MHz) used in non-linear microscopy, it matches the repetition rate of fast regenerative amplifiers. The gain in peak power afforded by regenerative amplification may indeed compensate for the lower duty cycle in many applications. This is particularly true for non-linear microscopy in biological tissue where amplified lasers enable deeper imaging depths [16-18]. By adding fast adaptive pulse shaping, AOD laser scanners may further improve deep tissue imaging by adaptive compensation of sample-induced aberrations to enhance the excitation focus beyond the scattering-limited transport length of excitation light in tissue. The most fundamental contribution of active beam shaping to microscopy is certainly the fast defocus. While an AOD lensing function was already successfully implemented into existing 3D microscopes [19-21], these implementations employ the counter-propagating-acoustic-wave configuration in four AODs for beam stabilization [4]. In comparison, the two-AOD plus AOM configuration offers the advantage of higher compactness, less exigent alignment, larger wavelength tunability and general beam shaping

function. AOD generated diffraction lenses have a zoom range of $\pm v^2 t_{access} / (\lambda f_{BW})$, according to Eq. (10). With f_{BW} = 35 MHz, λ = 840 nm, t_{access} = 10.3 µs, the focal range will be -15 to +15 cm. Therefore the lens can contribute a correction of up to ± 6.8 dioptres, reprogrammable from pulse to pulse, to the optical power of a microscope objective. In combination with an objective of 20x magnification and 9 mm focal length, for instance, this will allow shifting the objective focus up to about ± 520 µm in axial direction when using the full acoustic bandwidth, or ± 260 µm using half of the bandwidth. In this way the focus maintains the high NA of the objective in agreement with the focalization requirements of non-linear microscopy [22,23]. Finally fast defocusing could be used to compensate for fast 3D sample movements during *in vivo* optical recordings.

To conclude, we have demonstrated a new AOD-based spatial beam shaper that allows spatial modulation at several tens of kHz up to 200 kHz. Beam shaping at such speed provides opportunities for 3D random-access scanning in non-linear-microscopy, including the possibility to correct aberrations independently for every scanned point.

Acknowledgments

This work has received support under the program « Investissements d'Avenir » launched by the French Government and implemented by the ANR, with the references: ANR-10-LABX-54 (Memolife), ANR-11-IDEX-0001-02 (PSL* Research University) and ANR-10-INSB-04-01 (France-BioImaging infrastructure). We are grateful to the IBENS Imaging Facility, which received the support of grants from the "Région Ile-de-France" (NERF N°2009-44 and NERF N°2011-45), the "Fondation pour la Recherche Médicale" (N° DGE 20111123023) and the "Fédération pour la Recherche sur le Cerveau - Rotary International France" (2011).